Measurement 256 (2025) 117986

Contents lists available at ScienceDirect

Measurement

journal homepage: www.elsevier.com/locate/measurement

Feasibility analysis of EIT-guided lung tumor tracking with prior information for robotic arm-assisted radiotherapy

Hao Yu [a,1], Hao Yu [c,2], Zhongxu Dong [d,2], Wei Han [e,1], Yang Wu [b,3], Chunpeng Wang [a,4], Zhe Liu [a,1], Jiabin Jia [a,*,5]

[a] School of Engineering, University of Edinburgh, Edinburgh, EH9 3JL, UK
[b] College of Mechanical and Electronic Engineering, Nanjing Forestry University, Nanjing 210037, China
[c] School of Mathematical and Computer Sciences, Heriot-Watt University, and with the School of Informatics, University of Edinburgh, Edinburgh EH8 9AB, UK
[d] James Watt School of Engineering, University of Glasgow, Glasgow, G12 8QQ, UK
[e] School of Computer Science and Informatics, Cardiff University, Cardiff CF24 4AG, UK

ARTICLE INFO

Keywords:
Electrical impedance tomography
Lung cancer diagnosis
Tumor localization
Tumor tracking
Robot-assisted radiotherapy
EIT-guided radiotherapy

ABSTRACT

Lung cancer remains one of the most prevalent and lethal forms of cancer worldwide. Radiotherapy is an effective therapeutic strategy for its management, where precise tumor localization plays a pivotal role in ensuring treatment accuracy and efficacy. Electrical Impedance Tomography (EIT), a non-invasive and cost-effective imaging technique with a high temporal resolution, shows promise for tissue abnormality detection by exploiting the inherent differences in electrical properties among biological tissues. In this study, we propose a method that combines EIT with prior information from X-ray Computed Tomography (XCT) to determine tumor position. The integrated localization data are then transferblack to a robotic arm, which uses this information to accurately guide radiotherapy procedures. The detailed system design of the EIT-guided robotic arm for radiotherapy is presented. Additionally, both simulations and water tank experiments are conducted to validate the feasibility of this approach. The results demonstrate the potential of integrating EIT with XCT and robotic systems for tumor localization and targeted radiotherapy, thereby broadening the clinical applications of EIT in the medical field.

1. Introduction

Lung cancer remains a leading cause of cancer-related mortality worldwide, with approximately 2.5 million new cases and 1.8 million deaths reported globally in 2022 [1]. Surgical resection of the tumor is widely recognized as the first-line treatment method. However, patients exhibiting comorbidities, compromised cardiopulmonary function, or personal reservations about surgical intervention may not be suitable candidates for this procedure [2]. Therefore, radiotherapy stands as a highly effective and widely adopted non-surgical treatment alternative.

One critical challenge associated with radiotherapy for lung cancer is accounting for respiratory-induced tumor motion. It has been documented that tumors in the lung may shift up to 3.5 cm due to respiration [3,4]. This movement inevitably results in radiation exposure of surrounding healthy tissues, subsequently causing undesiblack cellular damage or death [5]. To address this problem, several approaches have been proposed, including adjusting dose volumes, administering protective pharmaceutical agents, and employing Image-guided Radiotherapy (IGRT) technologies [6]. Among these strategies, IGRT stands out as a particularly promising solution, enabling real-time tumor tracking and adjustment of radiation beams to precisely target the moving tumor [7–9].

Current imaging modalities typically employed for IGRT include Magnetic Resonance Imaging (MRI) and Computed Tomography (CT), both offering high spatial resolution. However, these techniques inherently possess relatively low temporal resolution, limiting their ability to provide real-time localization of tumors during radiation delivery [10].

* Corresponding author.
E-mail addresses: h.yu@ed.ac.uk (H. Yu), s2273711@ed.ac.uk (H. Yu), z.dong.2@research.gla.ac.uk (Z. Dong), HanW6@cardiff.ac.uk (W. Han), wuyang@njfu.edu.cn (Y. Wu), s2613747@ed.ac.uk (C. Wang), s1882383@sms.ed.ac.uk (Z. Liu), jiabin.jia@ed.ac.uk (J. Jia).
[1] Currently a Postdoc.
[2] Currently a Ph.D. degree candidate.
[3] Currently a lecturer.
[4] Currently an undergraduate student.
[5] Currently a Senior Lecturer and PhD candidate supervisor.

https://doi.org/10.1016/j.measurement.2025.117986
Received 1 April 2025; Received in revised form 6 May 2025; Accepted 26 May 2025
Available online 13 June 2025

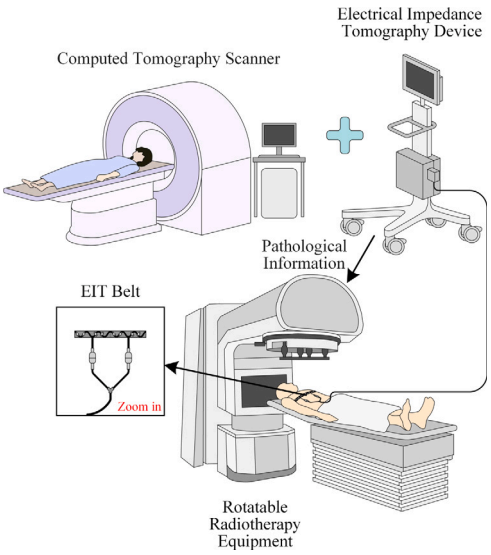

Fig. 1. Schematic of the proposed lung tumor tracking system guided by EIT with prior information from X-ray computed tomography.

Consequently, there remains a critical need for imaging methods with higher temporal resolution, and cost-efficiency.

Recently, Electrical Impedance Tomography (EIT), an emerging medical imaging technology, has attracted significant attention due to its advantages of high temporal resolution, safety, and affordability [11–13]. In pulmonary applications, EIT provides continuous, real-time bedside monitoring and has the potential to personalize ventilator settings as well as monitor the effects of PEEP titration [14]. Furthermore, EIT can be utilized to assess regional expiratory time constants during forced vital capacity maneuvers, enabling the early detection of lung function impairment even in individuals with normal spirometry results [15]. Beyond pulmonary applications, EIT has also shown promise in oncology, including breast tumor detection [16] and integration into high-dose-rate brachytherapy, as demonstrated in soft-tissue simulation studies conducted by Tan et al. [17]. These advancements suggest the feasibility of further expanding EIT applications in radiotherapy to address challenges in lung tumor motion tracking.

Inspiblack by these developments, this study proposes a novel integrated prototype system that uses the real-time capabilities of EIT in conjunction with prior anatomical information obtained via X-ray Computed Tomography (XCT) imaging to track the tumor movement due to respiration. This combined approach aims to accurately localize lung tumors during respiratory motion, subsequently guiding a robotic arm-assisted radiotherapy system, as illustrated in Fig. 1. To verify the practicality and effectiveness of the proposed method, comprehensive simulation studies and water tank experiments have been conducted. The key contributions of this work can be summarized as follows: (1) Integrating EIT with XCT-derived prior information facilitates tumor localization with high temporal resolution. (2) Based on the new localization method, the integrated robotic arm prototype agilely tracks tumor motion during radiotherapy. (3) Simulations and experiments validate the feasibility of the proposed method.

The remainder of this paper is organized as follows. Section 2 introduces the mathematical models of the EIT system and the robotic arm, and presents the overall methodological pipeline. Simulations and water tank experiments are carried out to demonstrate the feasibility of the EIT-guided lung tumor tracking approach in Sections 3 and 4, respectively. In addition, Section 4 discusses the limitations of the current work. Finally, Section 5 concludes the paper.

2. Methodology

2.1. EIT principles and tumor localization

2.1.1. EIT forward problem

Consider an imaging domain $\Omega \subset \mathbb{R}^D$, where $D = 2$ or 3, L electrodes, denoted as $\{e_i\}_{i=1}^{L}$, are uniformly distributed along its boundary $\partial\Omega$. When the excitation current $I(p)$ is inserted into the domain, according to the law of Kirchhoff and the electromagnetic equations of Maxwell, the relationship [18] between continuous, real-valued conductivity distribution $\sigma(p)$ and induced potential distribution $u(p)$ follows the following partial differential equation:

$$\nabla \cdot [\sigma(p)\nabla u(p)] = 0, \quad p \in \Omega \tag{1}$$

The associated boundary conditions are given by:

$$\begin{aligned} &u(p) + z_i\sigma(p)\frac{\partial u(p)}{\partial n} = U_i, && p \in e_i, \quad i = 1, 2, \ldots, L \\ &\int_{e_i} \sigma(p)\frac{\partial u(p)}{\partial n} dS = I_i, && i = 1, 2, \ldots, L \\ &\sigma(p)\frac{\partial u(p)}{\partial n} = 0, && p \in \partial\Omega \setminus \bigcup_{i=1}^{L} e_i \\ &\sum_{i=1}^{L} I_i = 0, \quad \sum_{i=1}^{L} U_i = 0. \end{aligned} \tag{2}$$

Here, $u(p)$ represents the electrical potential within the given region, and n denotes the outward unit normal to $\partial\Omega$. The parameters z_i, U_i, and I_i correspond to the contact impedance, electrical potential, and injected current at the electrode e_i, respectively. The forward problem in EIT is typically solved using the Finite Element Method (FEM). Among various excitation and measurement strategies, the adjacent pattern is widely used due to its ability to provide independent measurements [19].

2.1.2. EIT inverse problem

The EIT inverse problem seeks to estimate the conductivity distribution from measublack boundary voltages [20]. To achieve this, the imaging domain is segmented into an inverse mesh, which is typically coarser than the forward mesh. We assume the domain is partitioned into N disjoint subregions, such that $\Omega = \bigcup_{n=1}^{N} \Omega_n$ where each subregion has a uniform conductivity. This assumption simplifies the problem by representing the conductivity distribution as a discrete vector $\sigma \in \mathbb{R}^N$. As a result, the nonlinear relationship between the discrete conductivity distribution and the complete EIT measurements $V \in \mathbb{R}^M$ can be expressed as follows:

$$V = F(\sigma) \tag{3}$$

where $F(\cdot)$ is the nonlinear forward operator, and V represents the measublack voltage. To linearize this equation, the following approximation is introduced:

$$\Delta V = S \cdot \Delta\sigma \tag{4}$$

where ΔV and $\Delta\sigma$ denote the voltage and conductivity variations after normalization; S is the sensitivity matrix, also known as the Jacobian matrix. Consequently, the EIT inverse problem can be formulated as:

$$\hat{\Delta\sigma} = \min_{\Delta\sigma} \frac{1}{2}\|S\Delta\sigma - \Delta V\|^2 + \eta Re(\Delta\sigma), \tag{5}$$

where $Re(\cdot) : \mathbb{R}^N \to \mathbb{R}$ denotes the regularization function, and $\eta > 0$ represents the regularization coefficient.

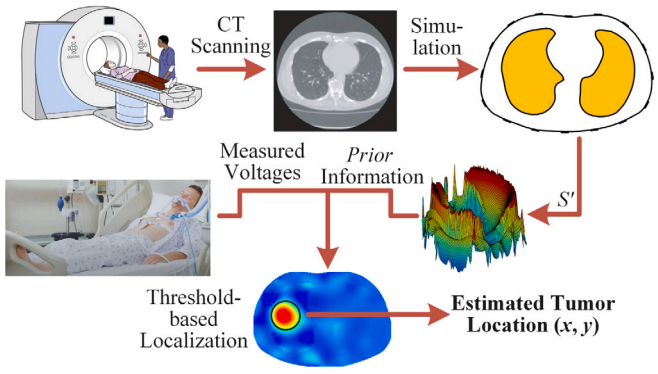

Fig. 2. Schematic diagram of lung tumor localization using the EIT+XCT method.

2.1.3. Tumor localization

Due to the inherent ill-posed nature and limited spatial resolution of EIT, the reconstructed images often struggle to accurately resolve lung tumors. Inspiblack by prior research [21], the "EIT+XCT" method, illustrated in Fig. 2, is proposed for reconstructing the lung tumor conductivity distribution. Only one shot of an axial XCT slice in the transverse plane, viewed from inferior to superior at the lung level, is sufficient for incorporating prior structural information in the proposed "EIT+XCT" method. This combined approach utilizes the complementary strengths of XCT, known for its high spatial resolution, and EIT, recognized for its real-time imaging capability. Specifically, prior anatomical information, including lung position, shape, and chest contour, is extracted from XCT images and subsequently incorporated into the reconstruction process for lung tumor localization.

First, to address the forward problem in EIT, the FEM is applied within the region Ω' containing the normal lung conductivity σ_{Lung}, whose shape is determined from prior anatomical information extracted from XCT images., and the corresponding sensitivity matrix S' is computed to substitute for the traditional empty sensitivity matrix S. Then, to balance the trade-off between imaging accuracy and computational efficiency, the Tikhonov regularization is employed. It is mathematically formulated as:

$$\Delta\sigma' = \left(S'^{T}S' + \lambda I\right)^{-1} S'^{T}\Delta V \tag{6}$$

where λ is the regularization parameter.

Finally, to quantify tumor locations and provide coordinates for the robotic arm, the centroid of regions with a relative conductivity exceeding a pblackefined threshold is computed, designating this point as the tumor center. The pblackefined threshold is determined empirically to balance detection sensitivity and specificity during tumor detection. Given that lung tumors typically exhibit higher conductivity compablack to normal lung tissue, EIT is particularly suitable for tumor detection and localization by effectively leveraging these conductivity differences along with the prior sensitivity matrix S'.

2.2. Kinematics and control of EIT-guided robot-assisted radiotherapy

2.2.1. Estimation of end-effector pose

After localizing the lung tumor with EIT, a robotic arm equipped with a radiotherapy end-effector will approach and track the tumor to perform radiation treatment. The EIT localization method first determines the tumor's center within the planar coordinate system defined by the EIT electrode array. After receiving the tumor position from the EIT system, the robotic arm estimates the target pose of the end-effector by following the principle of minimizing the distance to the tumor. In other words, along with the chest contour and lung-related information obtained by XCT, the robotic arm guides the end-effector to approach the tumor as closely as possible without compressing the thorax. The robot also aligns the radiotherapy end-effector with the tumor's center and dynamically tracks the tumor's movement caused by respiratory movements. The end-effector's pose, estimated in the EIT coordinate system, must be transformed into the Cartesian coordinate system of the robot's workspace for robot control.

$$T_r = {}^{r}T_e \begin{bmatrix} R_e & P_e \\ 0 & 1 \end{bmatrix} \tag{7}$$

where R_e and P_e are the orientation matrix and position vector of the end-effector in the EIT coordinate system, respectively. ${}^{r}T_e$ is the transformation matrix between the EIT and robot coordinate systems. T_r is the end-effector pose matrix in the robot Cartesian coordinate system, which can also be computed through the orientation and position coordinates:

$$T_r(x, y, z, \alpha, \beta, \gamma) = \begin{bmatrix} R_{11} & R_{12} & R_{13} & x \\ R_{21} & R_{22} & R_{23} & y \\ R_{31} & R_{32} & R_{33} & z \\ 0 & 0 & 0 & 1 \end{bmatrix} \tag{8}$$

where $R_{11} = c(\alpha)c(\beta)$, $R_{12} = -c(\gamma)s(\alpha) + c(\alpha)s(\beta)s(\gamma)$,
$R_{13} = s(\alpha)s(\gamma) + c(\alpha)c(\gamma)s(\beta)$,
$R_{21} = c(\beta)s(\alpha)$, $R_{22} = c(\alpha)c(\gamma) + s(\alpha)s(\beta)s(\gamma)$,
$R_{23} = -c(\alpha)s(\gamma) + c(\gamma)s(\alpha)s(\beta)$,
$R_{31} = -s(\beta)$, $R_{32} = c(\beta)s(\gamma)$, $R_{33} = c(\beta)c(\gamma)$.

x, y and z are the position coordinates; α, β, and γ are the orientation coordinates. s and c are sine and cosine functions, respectively. The end-effector posture vector in the robot coordinate system can therefore be calculated from the pose matrix, which is:

$$\boldsymbol{q} = [x, y, z, \alpha, \beta, \gamma] \tag{9}$$

2.2.2. Trajectory planning

In the robot-assisted radiotherapy scenario, the human body remains stationary on the bed; the chest contour is known in the robot workspace. Given these conditions, we adopt the Rapidly-Exploring Random Trees (RRT) algorithm [22] to plan the motion trajectory of the robotic arm from the initial position and radiotherapy position. Based on the initial and target posture vectors of the end-effector, the RRT searches for suitable path points in the six-dimensional configuration space, where the human body is modeled as an obstacle area. Each determined path point is a six-dimensional posture vector. We use a sampling step size of 5 cm and a maximum of 1000 iterations. The human chest is modeled as a static cylindrical obstacle based on prior XCT scans. The goal is defined by the tumor center localized from the EIT reconstruction. A path is accepted if it maintains a minimum clearance of 1 cm from the chest boundary. B-splines interpolation algorithm [22] is further employed to generate a continuous and more smooth spatial path (one waypoint per centimeter). We balance smoothness and latency by limiting the spline degree to 3 and ensuring that all interpolated waypoints remain within the robot's reachable and collision-free configuration space. Joint angle limits are strictly enforced during path validation by rejecting any intermediate posture exceeding the robot's joint limits. The spatial path is then converted into a time-parameterized form to construct the velocity profile.

2.2.3. Forward and inverse kinematics

The velocity profile in Cartesian space must be transformed into joint space for joint motor control through forward and inverse kinematics algorithms. The forward kinematic model of the real-time robotic arm posture needs be first derived with the Denavit-Hartenberg convention [23], and then used for calculating the Jacobian matrix. The Levenberg–Marquardt algorithm [24] is employed to address the

inverse kinematics problems. This algorithm incorporates a damping factor, denoted as λ_R, to improve the numerical stability. The mathematical expression is presented as follows:

$$\dot{\theta}(t) = J^T \left(JJ^T + \lambda_R^2 I_R \right)^{-1} \dot{q}(t) \tag{10}$$

Here, J represents the Jacobian matrix of the robot, while $\dot{\theta}(t)$ correspond to the joint velocities profiles. The pseudo code for the approaching movement is as Algorithm 1.

Algorithm 1 EIT-Guided Robot-assisted Radiotherapy

Require: Target pose $\mathbf{P}_e$, $\mathbf{R}_e$ and ${}^{r}T_e$
Require: Initial joint config $\mathbf{q}_{\text{init}}$, PID gains (K_p, K_i, K_d)
Require: Real-time joint positions $\theta(t)$
Step 1: Coordinate Transformation
$\mathbf{T}_r \leftarrow \mathbf{P}_e$. $\mathbf{R}_e$ and ${}^{r}T_e$
$\mathbf{q}_{goal} = [x, y, z, \alpha, \beta, \gamma] \leftarrow \mathbf{T}_r$

Step 2: RRT Path Planning
Initialize RRT from $\mathbf{q}_{\text{init}}$
while $\mathbf{q}_{goal}$ not reached **do**
    Sample $\mathbf{T}_{\text{sample}}$
    if collision-free and valid **then**
        Add node to tree
    end if
end while
Extract path $\mathcal{P}_{\text{raw}}$

Step 3: B-spline Smoothing
Interpolate $\mathcal{P}_{\text{raw}}$ to get $\mathcal{P}_{\text{smooth}} = \{\mathbf{q}_1, \ldots, \mathbf{q}_k\}$
Validate each point for collision and joint limits
Set desiblack end-effector speed $v_{\max} = 1$ cm/s
Compute time-parameterized velocity profile $\dot{\mathcal{Q}} = \{\dot{\mathbf{q}}_1, \ldots, \dot{\mathbf{q}}_k\}$ with timestamps $\{t_1, \ldots, t_k\}$.

Step 4: Approaching Movement
for $\dot{\mathbf{q}}_i$ in $\dot{\mathcal{Q}}$ **do**
    $J \leftarrow$ Forward Kinematics$(\theta(t))$
    $\dot{\theta}(t) \leftarrow$ Inverse Kinematics$(J, \dot{\mathbf{q}}_i)$
    sent $\dot{\theta}(t)$ to controller
end for

Step 5: Posture Correction
while radiotherapy is conducting **do**
    $\mathbf{q}(t)$, $J \leftarrow$ Forward Kinematics$(\theta(t))$
    compute error $\Delta\mathbf{q} = \mathbf{q}_{goal} - \mathbf{q}(t)$
    $\Delta\theta \leftarrow$ Inverse Kinematics$(J, \Delta\mathbf{q})$
    Send $\Delta\theta$ to controller
    Repeat updated $\mathbf{q}_{goal}$
end while

2.2.4. Real-time posture correction guided by EIT

After the radiotherapy end-effector mounted on the robot reaches the target position, it is also necessary to adjust the pose of the end-effector in real time according to the rhythmic position change of the lung tumor during breathing. The EIT system determines the real-time position of the tumor in the chest and transmits this information to the robotic system. Based on the aforementioned forward and inverse kinematics algorithm, the robot adjusts its posture with a Proportional–Integral–Derivative position controller to maintain a constant relative pose between the end-effector and the tumor. The tuned gains are set as: $K_p = 0.6$, $K_i = 0.1$, $K_d = 0.05$, empirically adjusted to ensure stable convergence without overshoot in the small workspace (1–2 cm range).

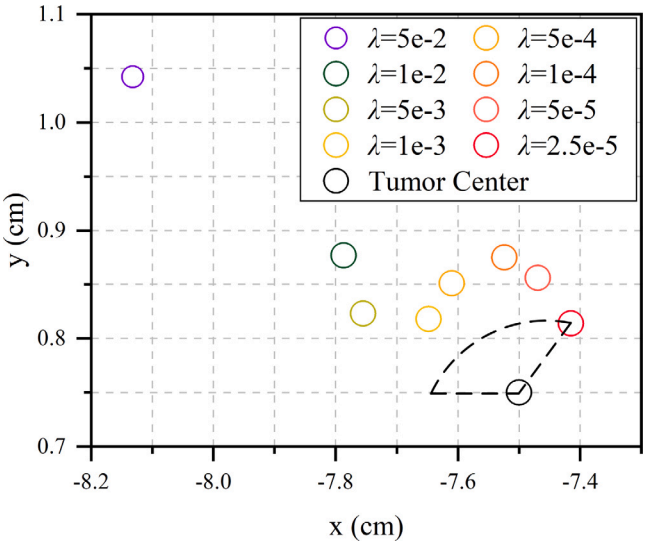

Fig. 3. Estimation of tumor position with different regularization parameters.

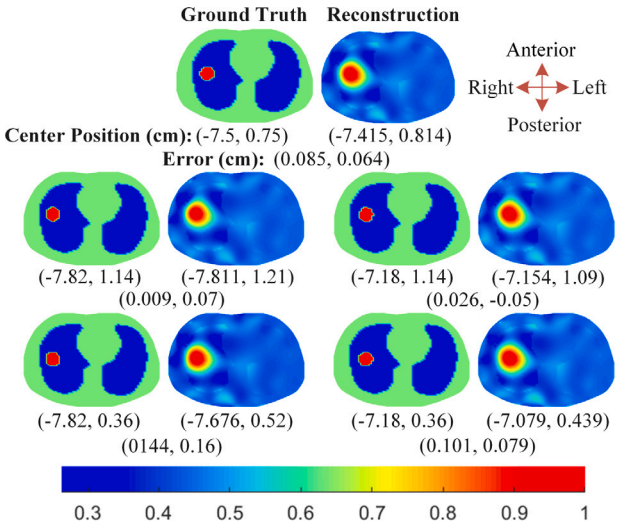

Fig. 4. Results of the conductivity distribution reconstruction and the estimation of tumor position in simulation.

3. Simulation results and analysis

The electrical conductivities of the background tissues and lungs are assigned based on their physiological properties [25], with values of 0.24 S/m for background tissues and 0.1 S/m for the lung. A higher conductivity of 0.38 S/m is assigned to the tumor region to reflect its distinct electrical characteristics.

In cases where lung abnormalities are present, such as the development of a tumor, the measublack boundary voltages, combined with prior anatomical information, can be employed to reconstruct the internal conductivity distribution. In this study, the tumor is modeled as a sphere with a diameter of 3 cm, and its center is designated as the tumor location.

3.1. Effect of the regularization parameter on tumor position estimation

In the employed Tikhonov reconstruction method, the regularization parameter λ plays a critical role in both conductivity distribution reconstruction and tumor localization. In the paper, λ is determined via a linear search, and the value that yields the smallest Euclidean distance

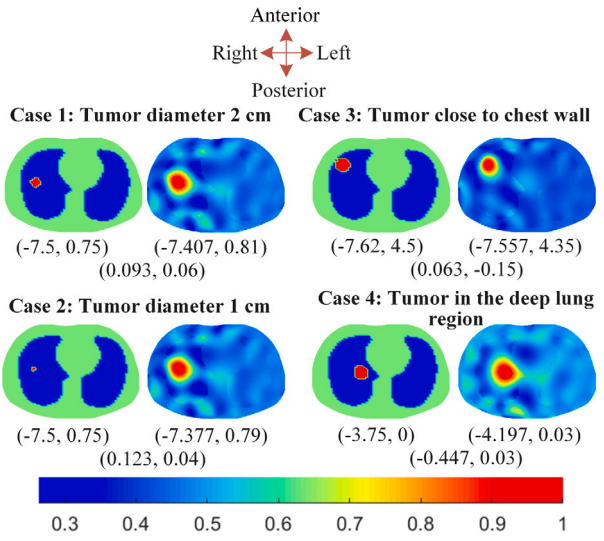

Fig. 5. Tumor localization results across varying sizes and locations.

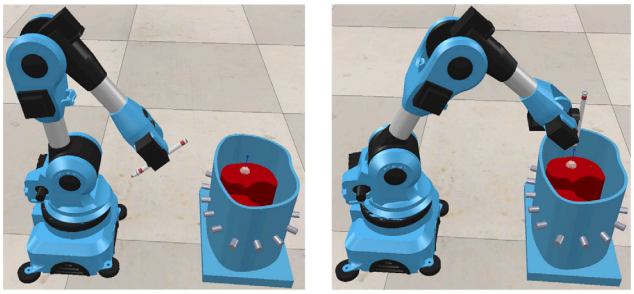

Fig. 6. EIT-guided robotic arm co-simulation. (a) Initial positioning; (b) Treatment phase with the end-effector accurately aligned for radiotherapy.

between the estimated tumor location and the ground truth is selected. The parameter tuning process is illustrated in Fig. 3. It is worth noting that, due to the ill-posed nature of the EIT problem, selecting smaller λ values within a certain range may blackuce the localization error but can also introduce artifacts in the reconstructed images. Taking these factors into account, a value of 2.5×10^{-5} is selected for conductivity reconstruction in the simulation.

3.2. Tumor conductivity reconstruction

The lung tumor exhibits motion due to respiratory activity, with a maximum displacement of up to 3.5 cm. Furthermore, according to [26], average tumor displacements during quiet respiration are 0.34 cm, 0.45 cm, and 0.72 cm in the upper, middle, and lower lung regions, respectively. Therefore, in the paper, similar average motion distances of 0.32 cm and 0.39 cm are adopted as examples for the right–left and anterior–posterior directions, respectively. Representative reconstruction results obtained using the Tikhonov regularization method are shown in Fig. 4. The estimated positions of the tumor center, as determined by EIT, exhibit consistent spatial patterns that align with the tumor's expected motion trajectory. Furthermore, Fig. 5 shows the tumor localization results across varying sizes and locations. From the figure, it can be observed that the proposed method is capable of accurately estimating the position of tumor with representative sizes (e.g., 2 cm in diameter) and also demonstrates good localization performance for smaller tumors with a diameter of only 1 cm. In addition, the method achieves reliable localization for tumors located both near the chest wall and deep within the lung. These results indicate that the proposed EIT-based localization approach exhibits generalization ability across various scenarios. Given that the modeled tumor has a radius of 1.5 cm, localization errors within this range are consideblack acceptable.

The localization errors observed in the simulation may be attributed to three main factors. First, the ill-posed nature of the EIT inverse problem limits the achievable spatial resolution, thereby introducing reconstruction errors. Second, although Tikhonov regularization improves the stability of the solution, it introduces a certain degree of computational bias due to the smoothing process. Finally, during tumor center extraction based on threshold segmentation, the potential presence of high-value artifacts in the reconstructed images is not fully accounted for, which further affected the localization accuracy. Overall, our quantitative analysis indicates that the proposed "EIT+XCT" approach demonstrates promising potential for accurate tumor localization, thereby supporting the feasibility of integrating EIT with a robotic arm for radiotherapy applications. It is worth noting that EIT employing only the Tikhonov method is unable to reconstruct the tumor without incorporating prior information about the lung shape.

3.3. Joint simulation of EIT and robotic arm

The collaborative simulation framework integrates COMSOL Multiphysics, MATLAB, and COPPELIASIM. COMSOL Multiphysics is used to acquire voltage measurements, while MATLAB is responsible for reconstructing the conductivity distribution, extracting the lung tumor position, and controlling the robotic arm. COPPELIASIM provides the virtual environment for simulating robotic operations. The system's performance under two scenarios, initial positioning and tracking, is illustrated in Fig. 6.

As shown in the figure, once information is obtained from the EIT+XCT framework, the system is capable of accurately tracking the tumor position. Specifically, voltage measurements simulated using COMSOL and processed in MATLAB are employed to reconstruct the conductivity distribution. Through thresholding and localization algorithms, the tumor position is identified. MATLAB then communicates with COPPELIASIM via virtual control to track the tumor in real time, thereby simulating the radiotherapy process.

4. Experimental setup and results

The feasibility and performance of the EIT-guided tumor tracking prototype system are assessed through a series of water tank experiments designed to emulate real-world scenarios in which lung tumors move due to respiration. These experiments also simulate the tumor radiotherapy process by regulating the motion of the robotic arm.

The experiments take place in a 30-cm-diameter water tank, where a 5-cm-diameter metal rod serves as a surrogate for the lung tumor. The tumor position is manually adjusted by moving the metal rod. The system reconstructs the conductivity distribution using the acquiblack voltage measurements. Subsequently, the laptop applies Gaussian convolution operations to extract precise positional data of the metal rod from the reconstruction results. This processed information is then transmitted to the robotic arm via a designated communication protocol, enabling the robotic arm to adjust its position and align its end-effector with the metal rod. Furthermore, in this experimental setup, an excitation frequency of 10 kHz and an excitation amplitude of 1 mA are applied.

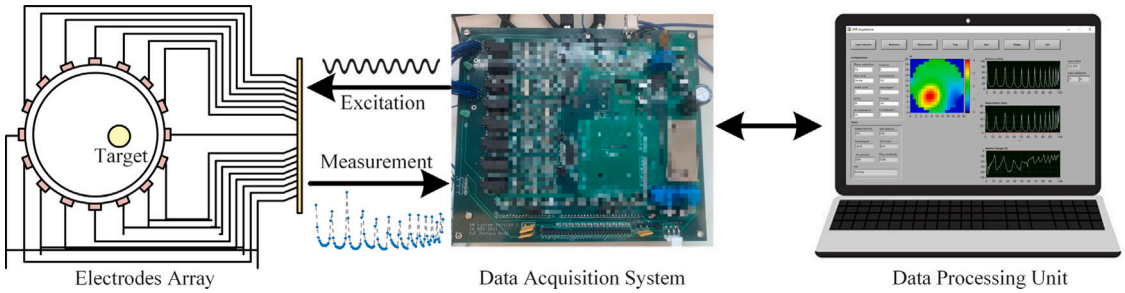

Fig. 7. Block diagram of the designed Edinburgh EIT system.

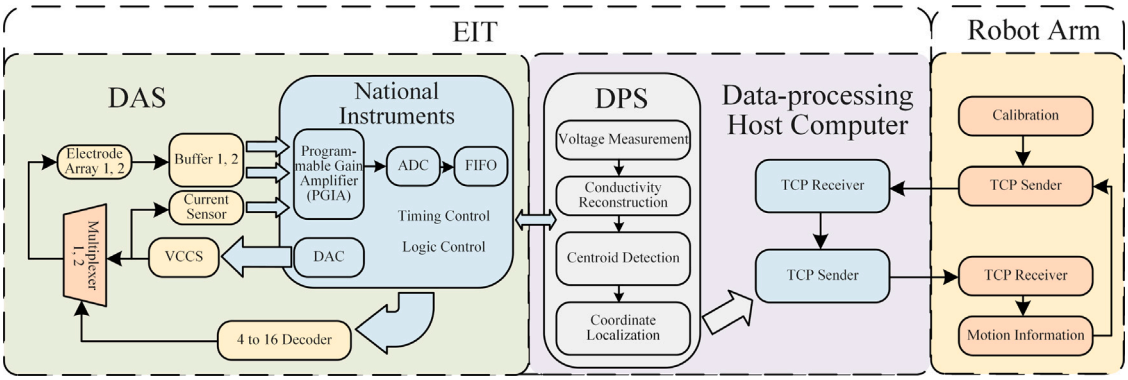

Fig. 8. Framework of the proposed Edinburgh EIT-guided robotic arm-assisted radiotherapy system.

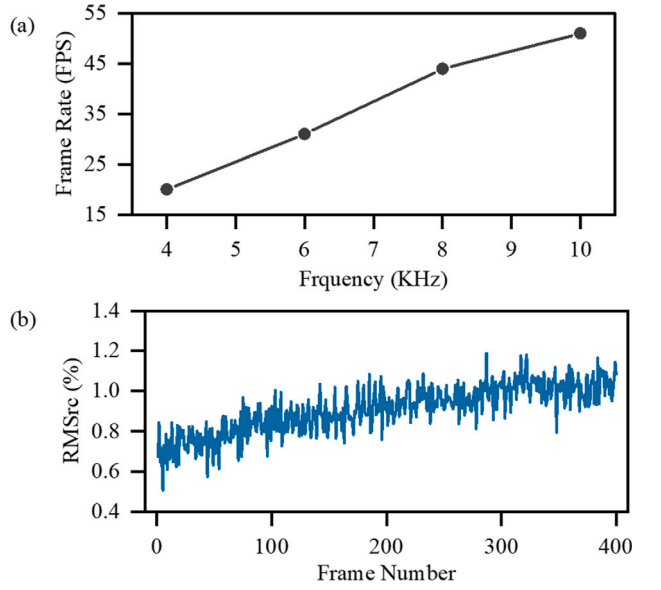

Fig. 9. Summary of performance metrics for the developed EIT system: (a) Frame rates at varying excitation frequencies; (b) RMS error over 400 frames at 10 kHz.

4.1. Prototype of the EIT-guided robotic arm system

4.1.1. Edinburgh EIT system

Fig. 7 presents the architecture of the proposed EIT system, which consists of three primary components: an electrode array, a data acquisition system, and a data processing unit. The electrode array includes 16 uniformly distributed electrodes.

The overall framework of the data acquisition system is illustrated in the left part of Fig. 8. The excitation module comprises a constant current source and a current monitoring circuit, which continuously measures the output current in real time. The current is deliveblack to selected electrode pairs through a set of multiplexer arrays. During each measurement cycle, the signal acquisition module collects 13 differential voltage signals from the remaining electrode pairs. These analog signals are first conditioned by a Programmable Gain Amplifier (PGIA) within the signal processing module to ensure appropriate signal levels. Subsequently, the conditioned signals are digitized via an analog-to-digital converter. The resulting digital data are then transmitted to the data processing unit through a USB 2.0 communication interface for further analysis and image reconstruction.

To evaluate the performance of the developed EIT system, two metrics temporal resolution, and repeatability are used. Repeatability reflects the consistency of the 16-channel measurements and is evaluated using the Root Mean Square of relative change (RMS_{rc}) between the reference and subsequent frames:

$$RMS_{rc} = 100\% \times \sqrt{\frac{1}{M}\sum_{i=1}^{M}\left(\frac{V_{Mea_i} - V_{Ref_i}}{V_{Ref_i}}\right)^2} \tag{11}$$

where V_{Mea_i} and V_{Ref_i} denote the ith voltage measurements in the measublack frame and the reference frame, respectively.

Results, as shown in Fig. 9, demonstrate the overall performance of the system. At an excitation frequency of 10 kHz, the system achieves a average frame rate of 51 fps, which meets the requirements for real-time lung imaging and enables responsive control of robotic arms. Furthermore, the RMS_{rc} is below 1.19%, suggesting excellent repeatability and measurement consistency.

4.1.2. Robotic arm

In this study, the Niryo One robotic arm [27], a 6-axis open-source robotic system developed in France, is selected as the controlled object. While simulation is performed through the integration of MATLAB and CoppeliaSim, the physical robot experiment is conducted without simulation software. In the experimental setup, the EIT module transmits tumor positions via the Transmission Control Protocol/Internet Protocol (TCP/IP) to a controller using the Niryo One SDK, enabling

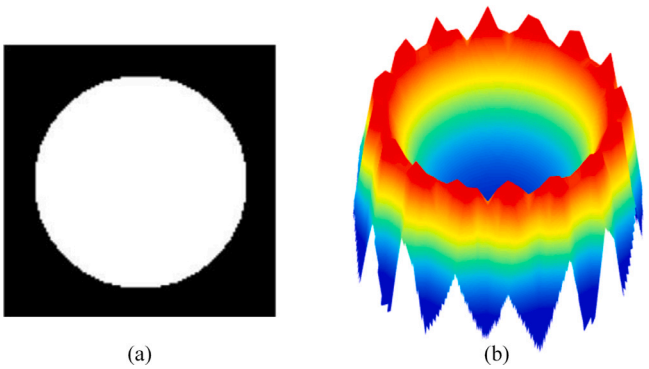

Fig. 10. (a) Simulated CT image of the water tank experiment; (b) Prior sensitivity matrix S'.

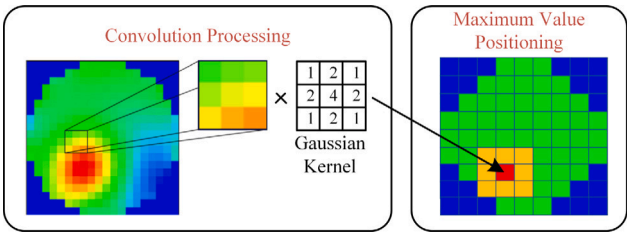

Fig. 11. Illustration of the Gaussian convolution process used in EIT to smooth reconstructed images.

real-time actuation of the robotic arm. TCP/IP, a standard for interconnecting heterogeneous systems, is employed to facilitate data exchange between the host PC and the robotic arm controller. As depicted in the block diagram on the left side of Fig. 8, the host PC operates as a TCP server: it reconstructs the EIT image, computes the corresponding target coordinates, and retains only the most recent value in a single-element buffer. Conversely, the robotic arm controller functions as a TCP client, periodically initiating a socket package to retrieve the current coordinates. Upon reception, the controller executes the prescribed motion and returns its updated state information to the host. This cyclical request–response mechanism establishes a closed-loop control architecture.

The total system delay is primarily influenced by the update frequency of the EIT system, the robot controller, and the TCP/IP communication latency. In our setup, the robotic control systems operate at 50 Hz, which is well within the acceptable range for real-time tumor tracking and significantly faster than the typical respiratory cycle frequency (0.25 Hz). However, due to an obvious communication delay, the average control cycle time for each posture correction is 2.66 s, according to our tests. This delay is acceptable in the water tank experiment, but it should be further shorten for periodic tumor displacement caused by actual respiratory cycle.

4.2. Target localization

In the experimental water tank setup, a 5-cm-diameter metal rod is employed to simulate a lung tumor, and the water tank is utilized to represent the chest. The simulated CT image and prior sensitivity matrix S' are presented in Fig. 10. The reconstructed conductivity distribution is depicted on a square grid comprising 20 × 20 pixels. Owing to the substantially higher electrical conductivity of the metal rod relative to the surrounding tap water, the EIT method could identify the positional information of the simulated tumor.

This paper adopts the Gaussian convolution method [28], motivated by its lower computational complexity, blackuced hardware resource requirements, and faster processing speed. The Gaussian convolution

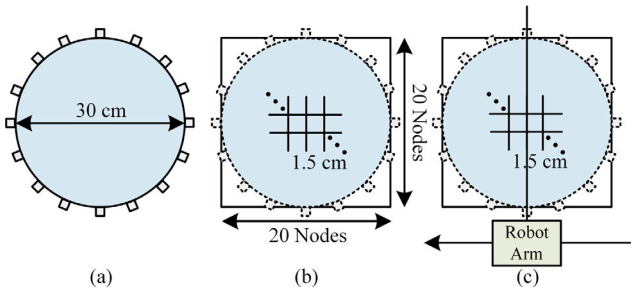

Fig. 12. Electrode layout and Cartesian grid mapping: (a) Circular water tank with 16 electrodes; (b) 20 × 20 conductivity grid with 1.5 cm spacing; (c) Mapping to Cartesian coordinates with robotic arm origin.

kernel functions as a spatial filter, effectively highlighting extreme conductivity values corresponding to the target position, as shown in Fig. 11. It should be specifically noted that the present study exclusively considers scenarios involving a single lung tumor.

The output value from the Gaussian convolution operation cannot be directly interpreted by the robotic arm as valid spatial information. Since the robotic arm performs path planning based on coordinate points in the Cartesian coordinate system, the index of the conductivity distribution must be mapped to a corresponding point in Cartesian space. The reconstructed conductivity distribution consists of 400 pixels, and the physical water tank is correspondingly divided into 400 virtual nodes. This establishes a one-to-one mapping between the conductivity distribution and the spatial grid of the tank. After mapping, each node is associated with a Cartesian coordinate, with the origin defined at the base of the robotic arm. The mapping process is illustrated in Fig. 12, where each node represents a 1.5 cm × 1.5 cm square within the water tank.

4.3. Experiment results

The schematic of the proposed experimental system is shown in Fig. 13, and the qualitative results of the EIT-guided robotic arm operation are illustrated in Fig. 14. As shown in Fig. 14, the robotic arm successfully tracks the metal rod, validating the effectiveness and practical feasibility of the proposed system. Sequential snapshots in Fig. 14 demonstrate the step-by-step movement of the robotic arm as it approaches and aligns with the target, guided by the position information provided by the EIT system.

5. Discussion and future research

5.1. Performance analysis and limitation

This study investigates the integration of EIT and XCT for accurate lung tumor localization, with the aim of guiding a robotic arm for precise radiotherapy delivery. Our findings highlight the critical impact of EIT sensor accuracy on the quality of input provided to the robotic arm control system. Although EIT achieves adequate temporal resolution for practical application, its limited spatial resolution remains a significant factor that could constrain the overall system performance. Furthermore, the precision control and rapid response capabilities of the robotic arm are closely associated with treatment efficacy and patient safety. The proposed integrated system holds considerable promise for enhancing the accuracy of lung cancer radiotherapy, blackucing radiation exposure to healthy tissues, and ultimately improving patient outcomes.

To evaluate the adaptability of the algorithm in multi-tumor scenarios, a simulation involving two tumors is designed to mimic the clinical requirement of localizing multiple lesions. A threshold-based

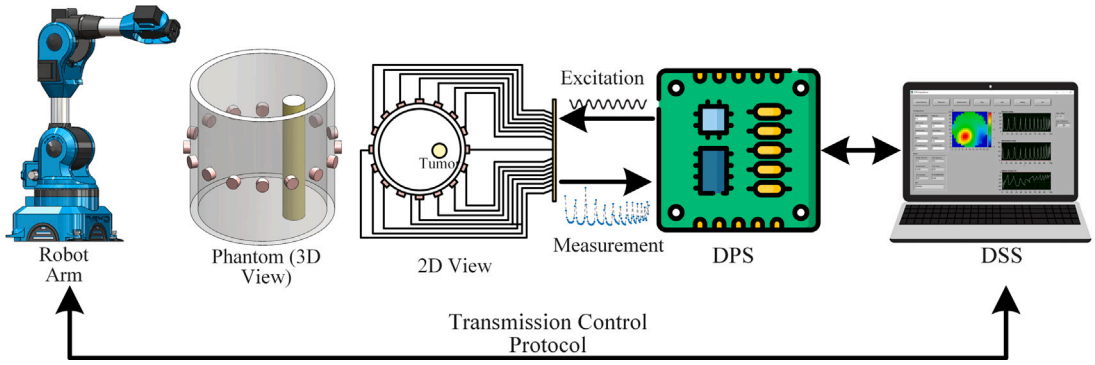

Fig. 13. Illustration of the experimental system. DPS: data processing system; DSS: digital analysis system.

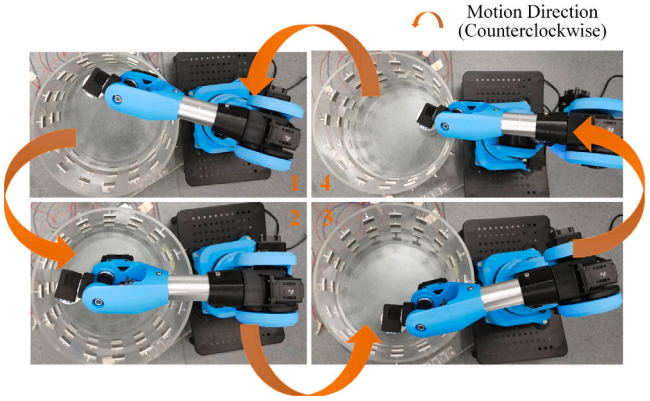

Fig. 14. Top-view snapshots of the prototype movement, showing different stages of the EIT-guided robotic arm operation. Orange arrows represent counterclockwise motion.

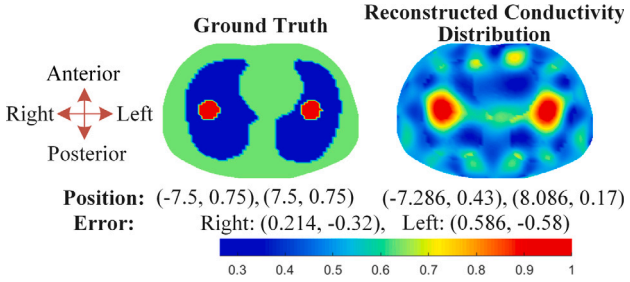

Fig. 15. Comparison of ground truth and reconstructed conductivity for a two-tumor case. Tumor positions and localization errors are shown to evaluate reconstruction accuracy.

multi-region segmentation algorithm is employed, combined with morphological processing to extract connected regions. Similarly, the tumor locations are determined by selecting the centroid of the largest connected component, as shown in Fig. 15. Compablack to the single-tumor case, the localization accuracy of EIT in the presence of bilateral lung tumors shows a slight decline, primarily due to the complex superposition of conductivity perturbations caused by multiple targets, which blackuces the accuracy of lesion separation during image reconstruction. For multi-lesion cases, a sequential irradiation strategy is adopted to ensure that each tumor receives an independent therapeutic response under the guidance of the control system.

5.2. Future work

Future research directions include conducting water tank experiments involving heterogeneous media, such as layeblack configurations representing lung, fat, and muscle tissues. Such experiments will enable a more rigorous evaluation of the method's applicability under conditions that better approximate the electrical impedance distribution of real biological environments. Moreover, extending the current two-dimensional framework to a fully three-dimensional system remains an essential step, particularly to account for respiratory-induced 3D tumor displacement. This extension would enable analysis of registration errors and tumor localization accuracy across varying respiratory phases.

From a hardware perspective, future work will involve replacing the current robotic arm with a high-precision collaborative robotic platform, such as the Franka Emika Research 3, which offers a factory-calibrated positioning accuracy of ±0.1 mm. In addition to enhanced accuracy, such platforms provide built-in force sensing and impedance control, which are critical for ensuring patient safety during human-in-the-loop interaction. On the software side, one priority is to address the unexpected latency observed in the current prototype system. Our analysis suggests that this delay is caused by suboptimal implementation of the TCP/IP communication protocol between the EIT localization module and the robotic controller. Refactoring the communication architecture, including using asynchronous messaging and buffer management, is expected to blackuce the total system latency to under 20 ms, making it compatible with real-time respiratory tracking.

Finally, improving the spatial resolution of EIT using data-driven reconstruction algorithms (e.g., deep learning) and enhancing the overall system temporal resolution through optimized robotic motion planning and control algorithms remain important avenues for advancing the clinical utility of the proposed approach.

6. Conclusion

In this study, we introduced a novel approach that integrates EIT with prior information from XCT for real-time lung tumor tracking and robotic arm-guided radiotherapy. Through simulations and water tank experiments, we confirmed the feasibility and effectiveness of our proposed method. The results indicate that the combination of EIT and XCT improves tumor tracking accuracy, providing reliable guidance for the robotic arm during precise radiotherapy procedures. This work not only demonstrates the expanded utility of EIT in medical applications but also highlights the considerable potential of integrating advanced imaging modalities and robotic systems in enhancing cancer treatment outcomes.

CRediT authorship contribution statement

Zhongxu Dong: Visualization, Project administration, Methodology, Investigation, Conceptualization. **Wei Han:** Validation, Methodology. **Yang Wu:** Writing – review & editing. **Chunpeng Wang:** Validation, Investigation. **Zhe Liu:** Validation, Project administration,

Methodology, Conceptualization. **Jiabin Jia:** Writing – review & editing, Supervision, Funding acquisition, Conceptualization. **Hao Yu:** Writing – original draft, Visualization, Validation, Software, Methodology, Investigation, Conceptualization. **Hao Yu:** Writing – original draft, Methodology, Conceptualization.

Declaration of competing interest

We state that this manuscript has not been published elsewhere and that it has not been submitted simultaneously for publication elsewhere.

We have no conflicts of interest to disclose.

Acknowledgment

The authors thank the School of Engineering at the University of Edinburgh for their kind support and insightful input during this study.

Data availability

Data will be made available on request.

References

[1] F. Bray, M. Laversanne, H. Sung, J. Ferlay, R.L. Siegel, I. Soerjomataram, A. Jemal, Global cancer statistics 2022: GLOBOCAN estimates of incidence and mortality worldwide for 36 cancers in 185 countries, CA: Cancer J. Clin. 74 (3) (2024) 229–263.

[2] H.J. Kang, Y.-K. Kwak, M. Kim, S.J. Lee, Application of real-time MRI-guided linear accelerator in stereotactic ablative body radiotherapy for non-small cell lung cancer: one step forward to precise targeting, J. Cancer Res. Clin. Oncol. 148 (11) (2022) 3215–3223.

[3] S. Park, S.J. Lee, E. Weiss, Y. Motai, Intra-and inter-fractional variation prediction of lung tumors using fuzzy deep learning, IEEE J. Transl. Eng. Heal. Med. 4 (2016) 1–12.

[4] P.J. Keall, G.S. Mageras, J.M. Balter, R.S. Emery, K.M. Forster, S.B. Jiang, J.M. Kapatoes, D.A. Low, M.J. Murphy, B.R. Murray, et al., The management of respiratory motion in radiation oncology report of AAPM task group 76 a, Med. Phys. 33 (10) (2006) 3874–3900.

[5] H.B. Stone, C.N. Coleman, M.S. Anscher, W.H. McBride, Effects of radiation on normal tissue: Consequences and mechanisms, Lancet Oncol. 4 (9) (2003) 529–536.

[6] P.R. Graves, F. Siddiqui, M.S. Anscher, B. Movsas, Radiation pulmonary toxicity: From mechanisms to management, in: Seminars in Radiation Oncology, vol. 20, Elsevier, 2010, pp. 201–207, 3.

[7] J. Yun, E. Yip, Z. Gabos, K. Wachowicz, S. Rathee, B. Fallone, Neural-network based autocontouring algorithm for intrafractional lung-tumor tracking using Linac-MR, Med. Phys. 42 (5) (2015) 2296–2310.

[8] N. Tahmasebi, P. Boulanger, J. Yun, G. Fallone, M. Noga, K. Punithakumar, Real-time lung tumor tracking using a CUDA enabled nonrigid registration algorithm for MRI, IEEE J. Transl. Eng. Heal. Med. 8 (2020) 1–8.

[9] A.P. Shah, P.A. Kupelian, B.J. Waghorn, T.R. Willoughby, J.M. Rineer, R.R. Mañon, M.A. Vollenweider, S.L. Meeks, Real-time tumor tracking in the lung using an electromagnetic tracking system, Int. J. Radiat. Oncol. Biol. Phys. 86 (3) (2013) 477–483.

[10] E. Lin, A. Alessio, What are the basic concepts of temporal, contrast, and spatial resolution in cardiac CT? J. Cardiovasc. Comput. Tomogr. 3 (6) (2009) 403–408.

[11] H. Yu, Z. Zhang, Y. Gao, J. Jia, Multiscale voltage reconstruction with attention-based network for volume fraction prediction of industrial oil–water two-phase flow by EIT, IEEE Trans. Instrum. Meas. 71 (2022) 1–9.

[12] A. Phisaiphan, P. Laor-Iam, C. Sukjamsri, A. Dowloy, T. Ouypornkochagorn, Bladder monitoring with time-frequency-difference electrical impedance tomography technique, Measurement (2025) 117162.

[13] H. Dong, X. Wu, D. Hu, Z. Liu, F. Giorgio-Serchi, Y. Yang, Learning-enhanced electronic skin for tactile sensing on deformable surface based on electrical impedance tomography, IEEE Trans. Instrum. Meas. (2025).

[14] G. Franchineau, A.H. Jonkman, L. Piquilloud, T. Yoshida, E. Costa, H. Rozé, L. Camporota, T. Piraino, E. Spinelli, A. Combes, et al., Electrical impedance tomography to monitor hypoxemic respiratory failure, Am. J. Respir. Crit. Care Med. 209 (6) (2024) 670–682.

[15] S. Qu, E. Feng, D. Dong, L. Yang, M. Dai, I. Frerichs, S. Liu, Y. Gao, J. Zheng, L. Song, et al., Early screening of lung function by electrical impedance tomography in people with normal spirometry reveals unrecognized pathological features, Nat. Commun. 16 (1) (2025) 622.

[16] J.C. Gómez-Cortés, J.J. Díaz-Carmona, J.A. Padilla-Medina, A.E. Calderon, A.I.B. Gutiérrez, M. Gutiérrez-López, J. Prado-Olivarez, Electrical impedance tomography technical contributions for detection and 3D geometric localization of breast tumors: A systematic review, Micromachines 13 (4) (2022) 496.

[17] H. Tan, C. Rossa, Electrical impedance tomography for robot-aided internal radiation therapy, Front. Bioeng. Biotechnol. 9 (2021) 698038.

[18] Z. Liu, Y. Yang, Multimodal image reconstruction of electrical impedance tomography using kernel method, IEEE Trans. Instrum. Meas. 71 (2021) 1–12.

[19] C. Dimas, P.P. Sotiriadis, Electrical impedance tomography image reconstruction for adjacent and opposite strategy using FEMM and EIDORS simulation models, in: 2018 7th International Conference on Modern Circuits and Systems Technologies, MOCAST, IEEE, 2018, pp. 1–4.

[20] Y. Wu, Y. Yu, H. Tian, Z. Li, H. Wang, K. Liu, J. Yao, Spatiotemporal residual recurrent neural network for lung function evaluation using electrical impedance tomography, IEEE Trans. Instrum. Meas. (2025).

[21] B. Sun, S. Yue, Z. Hao, Z. Cui, H. Wang, An improved Tikhonov regularization method for lung cancer monitoring using electrical impedance tomography, IEEE Sens. J. 19 (8) (2019) 3049–3057.

[22] K.M. Lynch, F.C. Park, Modern Robotics: Mechanics, Planning, and Control, first ed., Cambridge University Press, USA, 2017.

[23] C. Klug, D. Schmalstieg, T. Gloor, C. Arth, A complete workflow for automatic forward kinematics model extraction of robotic total stations using the Denavit-Hartenberg convention, J. Intell. Robot. Syst. 95 (2019) 311–329.

[24] J.J. Moré, The Levenberg-Marquardt algorithm: Implementation and theory, in: Numerical Analysis: Proceedings of the Biennial Conference Held At Dundee, June 28–July 1, 1977, Springer, 2006, pp. 105–116.

[25] H. Yu, H. Liu, Z. Liu, Z. Wang, J. Jia, High-resolution conductivity reconstruction by electrical impedance tomography using structure-aware hybrid-fusion learning, Comput. Methods Programs Biomed. 243 (2024) 107861.

[26] C. Plathow, S. Ley, C. Fink, M. Puderbach, W. Hosch, A. Schmähl, J. Debus, H.-U. Kauczor, Analysis of intrathoracic tumor mobility during whole breathing cycle by dynamic MRI, Int. J. Radiat. Oncol. Biol. Phys. 59 (4) (2004) 952–959.

[27] G. Nantzios, N. Baras, M. Dasygenis, Design and implementation of a robotic arm assistant with voice interaction using machine vision, Automation 2 (4) (2021) 238–251.

[28] P. Getreuer, A survey of Gaussian convolution algorithms, Image Process. Line 2013 (2013) 286–310.